nature communications

Article

https://doi.org/10.1038/s41467-026-69253-y

Axially engineered single atoms in enzyme-mimic-binding pocket steering dehalogenation–polymerization pathways toward water pollutant upcycling

Received: 6 September 2025

Accepted: 27 January 2026

Published online: 05 February 2026

Check for updates

Bin Wu[1], Zhiling Li[1] ✉, Jie Zhang[1], Weiyu Zhou[1], Shih-Hsin Ho[1], Xiaoguang Duan[2] ✉ & Aijie Wang[1,3] ✉

Polymerization-based advanced oxidation processes (P-AOPs) represent a promising strategy for simultaneous pollutant abatement and water resource recovery. However, selective removal of halogenated organic pollutants via P-AOP remains challenging due to uncontrollable oligomerization pathways and radical chain inhibition induced by the chlorine substituent. Here, we develop an axial-nitrogen-coordinated single-atom iron catalyst (Fe-NCN) that triggers an electron-transfer pathway (ETP) via enhanced electronic pulling on 2,4,6-trichlorophenol (TCP), achieving near-complete dechlorination and catalytic transformation into polymeric products. Spectroscopic characterization and theoretical calculations reveal that the axial coordination of Fe-NCN regulates peroxymonosulfate (PMS) activation to form surface PMS* complex, which oxidizes the adjacent TCP via a short-range ETP regime due to the charge-constrained nature of the carbon nitride substrate. Upon electron extraction from TCP, PMS* is transformed into an active surface hydroxyl intermediate (OH^{-}*), which attains nucleophilic substitution of organochlorine, subsequently triggering C-O crosslinking of the hydroxylated by-products with ultra-high electron utilization efficiency (~353%). This integrated dechlorination-hydroxylation-polymerization process can be scaled up for device-scale wastewater treatment with excellent stability. The collected oligomers can be processed to manufacture industrial-grade plastic products. This study advances the understanding of the complex polymerization regime of chlorinated micropollutants by using engineered atomic catalysts for sustainable and low-emission water purification.

Chemical oxidation technologies utilize generated reactive oxygen species (ROS) for effective degradation and mineralization of recalcitrant organic pollutants, demonstrating considerable potential for securing potable and drinking water supplies[1,2]. However, conventional mineralization-based advanced oxidation processes are limited by excessive oxidant dosages, toxic by-products (e.g., disinfection by-products), and excessive carbon emissions, collectively leading to higher treatment costs, secondary pollution risks, and excessive chemical consumption[3–5]. In contrast, polymerization-based advanced oxidation processes (P-AOPs) emerge as a sustainable alternative via

A full list of affiliations appears at the end of the paper. ✉e-mail: lizhiling@hit.edu.cn; xiaoguang.duan@adelaide.edu.au; wangaijie@hit.edu.cn

transforming aqueous organic pollutants into recyclable solid-phase products through selective catalytic pathways, enabling concurrent contaminant removal and resource recovery[6–9]. Nevertheless, the technical bottlenecks that constrain their practical implementation lie in the precise control of pollutant and product selectivity as well as long-term stability of the catalytic system.

Conversion efficiency in P-AOPs systems is predominantly governed by the electronic characteristics of substituents in parent compounds[10]. For example, halogenated phenols demonstrated substantially lower polymerization rates compared with their alkyl-substituted analogs[6,11]. This is because the strong electron-withdrawing (electronegativity) nature of halogen functionalities greatly delocalizes π-electron density away from the aromatic benzene, thereby destabilizing organic radical intermediates and kinetically impeding chain propagation of halogenated organic pollutants (HOPs)[10,11]. Furthermore, halogen substitution on the aromatic rings preferentially induced C-C coupling over C-O linkages[6,12–14]. The resultant C-C coupled products exhibit weaker interfacial interactions with catalytic surfaces because of the exposure of more polar oxygen functional groups[14], leading to enhanced aqueous phase mobility (Supplementary Fig. 1). Critically, these oligomeric species retain significant halogen content stemming from precursor molecules, amplifying their ecotoxicological potential through bioaccumulation[6,15]. Developing C-O linkages via dehalogenation synergistically enhances polymerization and detoxification of HOPs, while precise catalyst engineering to achieve controlled dehalogenation to produce high-quality polymerization substrate remains a critical bottleneck.

In hydrolytic enzymes, such as esterases in nature, the active centers use deprotonated H_2O (OH^-) as a nucleophilic reagent to attack electrophilic atoms in the substrate molecule to generate alcohols or acids[16]. Notably, halogen substituents amplify the electrophilicity of the adjacent carbon, creating activated (positively charged) sites for targeted nucleophilic substitution[17]. Similarly, surface-confined hydroxyl species, generated from catalytic cleavage of the peroxide bond in peroxymonosulfate (PMS), exhibit exceptional nucleophilicity, enabling direct nucleophilic attack or mediated indirect nucleophilic substitution of phenolic pollutants to yield hydroxyl groups[18]. The formation of phenolic hydroxyl groups not only enhances the stability of organic radical intermediates but also provides additional reactive crosslinking sites, promoting the subsequent C-O coupling-mediated polymerization[19]. Thus, modulating the electron transfer pathway (ETP) via the dual-electron process can activate PMS to generate surface-confined OH^- species (OH^{-*}), which may achieve oxidative conversion of recalcitrant chlorinated pollutants and intermediates via successive dehalogenation-hydroxylation-polymerization (DHP) processes.

Herein, we synthesize a mimic-enzyme axially ligand-modified single-atom iron catalyst (Fe-SACs, designated Fe-NCN), which achieves near-complete dehalogenation (99.3%) and polymerization transfer (98.2%) of 2,4,6-trichlorophenol (TCP). The electron-pulling effect of the axial nitrogen ligand modulates the electronic structure of the central Fe atoms, induces PMS coordination to form a complex intermediate (PMS*), and achieves rapid TCP removal by short-range ETP under the charge confinement of the substrates (k_{Nor} = 3.97 min^{-1} L g^{-1}). Integrated product identification, spectroscopic analysis, and density functional theory (DFT) calculations elucidate the role of axial ligands in regulating the catalytic pathway transition from singlet oxygenation to ETP, which facilitates the C-O crosslinking via the DHP path. In addition, mimicking the hydrophobic and polar microenvironment of the enzyme-binding pocket drives the separation of polar group-containing but macroscopic hydrophobic oligomers in the active site, thereby maintaining the catalyst activity. Combined techno-economic analysis (TEA), life cycle assessment (LCA), and continuous-flow reactor trials demonstrate the feasibility of industrial-scale manufacturing of Fe-NCN, robust wastewater treatment performance (TOC removal >80% within 60 days), carbon recovery potential (product recovery ≈ 45%) and environmental friendliness (carbon footprint decreased by 78%) in practical wastewater remediation.

Results

Synthesis and characterization of Fe-SACs

The structure and function of CYP152 peroxidase were fully dissected to design dehalogenation-polymerization catalysts. Microbial-mediated hydrolytic dechlorination occurs at the active center of heme iron modified by weakly axial sulfate ligands, using surface-activated peroxides to reconfigure the local hydrogen-bonding network for hydroxylated dehalogenation of the substrate (Fig. 1a)[18]. Binding pockets consisting of hydrophobic amino acids and polar-interacting residues provide substrate-trapping zones. B12-dependent reductive dehalogenases have also been reported to have similar structures[20] (Supplementary Fig. 2). Inspired by the structure of the natural enzyme, the introduction of axial ligands to modify the metal center may be beneficial for regulating the switch in oxidative mechanisms in the DHP pathway.

A pre-coordination-assisted strategy was used to prepare Fe-NCN, as shown in Fig. 1b. Initially, Fe^{2+} ions were complexed with 1,10-phenanthroline in aqueous solution to form a metal-organic precursor as pre-coordination templates. Subsequently, this complex was introduced into a graphitized carbon nitride (g-C_3N_4, CN) dispersion and subjected to ultrasonic treatment, followed by overnight aging to achieve oriented assembly of nanostructures. The products were treated by pyrolysis under NH_3/HCl atmosphere (generated from in situ hydroxylamine hydrochloride decomposition) to yield the porous carbon-supported single-atom iron catalyst (Fe-NCN). For comparative analysis, Fe-CN was synthesized in parallel using only iron salts as precursors. Scanning electron microscopy (SEM) and high-resolution transmission electron microscopy (HR-TEM) images revealed a hierarchical architecture of Fe-SACs with no visible Fe clusters or nanoparticles (Supplementary Fig. 3). Brunauer-Emmett-Teller (BET) analysis confirmed the incorporation of Fe species maintained the mesoporous structure of the CN substrate and significantly increased the specific surface area (SSA) of Fe-SACs (Supplementary Fig. 4). X-ray diffraction (XRD) patterns showed characteristic CN diffraction peaks without crystalline iron phases, ruling out the existence of Fe-based nanoparticles (Supplementary Fig. 5a)[21]. Atomic-resolution high-angle annular dark-field scanning transmission electron microscopy (AC-HAADF-STEM) directly visualized isolated Fe atoms as bright spots on the CN matrix (Fig. 1d and Supplementary Fig. 5b). Elemental mapping images verified homogeneous distribution of C, N, and Fe atoms throughout the CN framework (Fig. 1c and Supplementary Fig. 5d). Besides, the atom-overlapping Gaussian-function-fitting results from AC-HAADF-STEM displayed additional spatial information concerning the atomically dispersed Fe centers (Fig. 1e and Supplementary Fig. 5c). Inductively coupled plasma optical emission spectroscopy (ICP-OES) quantified Fe contents as 1.85 wt% and 2.06 wt% for Fe-CN and Fe-NCN, respectively (Supplementary Table 1). Notably, Fe-NCN synthesized using a pre-coordinated template showed a product yield of up to 45.0% and a more compact stacking of structures compared to Fe-CN (32.2%) (Supplementary Fig. 3). Thus, the pre-coordinated templating approach not only inhibits the loss of carbon and nitrogen at high temperatures through interlayer crosslinking, but also enables precise tuning of catalyst structures.

The coordination structure of Fe species was investigated using X-ray photoelectron spectroscopy (XPS). The absence of Fe–C and Fe–O bonds in Fe-SACs was confirmed by C 1s and O 1s XPS spectra (Supplementary Figs. 6 and 7). Deconvoluted N 1s spectra revealed characteristic Fe–N peaks at 399.2 eV in Fe-SACs with diminished pyridinic N signals compared to pristine CN, implying their chemical bonding with Fe species (Supplementary Fig. 8a)[22]. Time-of-flight secondary ion mass spectrometry (TOF-SIMS) at m/z = 67.93 and 71.94

https://doi.org/10.1038/s41467-026-69253-y

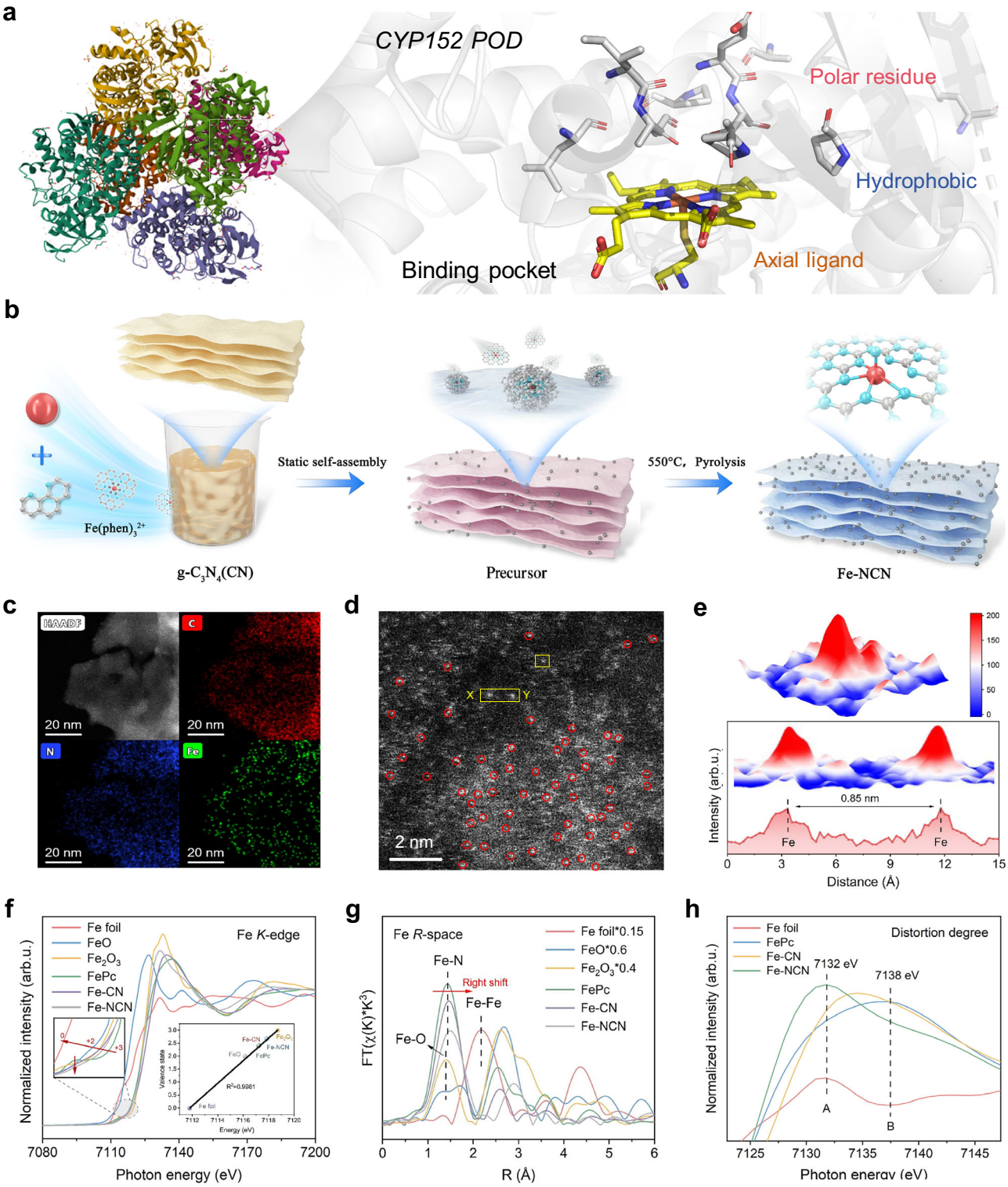

Fig. 1 | Composition characteristics, local coordination environment and electronic structure of catalyst. a Overall structure of CYP152 Peroxygenases (POD, P450 BS beta mutant F46A, Protein Data Bank ID: 9IY1). Amino acid fragments act as axial ligands that modulate the oxidative valence of the metal center, facilitating the promotion of oxidant activation, substrate recognition binding and maintenance of enzyme activity. The binding pocket consists of hydrophobic amino acid residues together with amino acid residues involved in polar interactions, providing a favorable microenvironment that not only promotes oxidant activation but also facilitates substrate binding and product release. For the enzyme model, light gray, carbon; red, oxygen; blue, nitrogen; reddish-brown, cobalt; yellow, carbon of the porphyrin ring. **b** Schematic diagram of catalyst synthesis process. For the model, red, iron; blue, nitrogen; light gray, carbon. **c** HAADF and EDS Mapping images and **d** ACHAADF-STEM images of the catalyst. **e** Atom-overlapping Gaussian-function-fitting mapping of the square and intensity profile along X-Y in (**d**). **f** XANES inset: magnification of local areas and fitting of oxidation valence and **g** FT-EXAFS spectra in R-space of Fe-SACs and reference samples at Fe K-edge. **h** The ratio I_A/I_B of the relative strengths of the two Fe K-edge eigenpeaks A and B present at 7132 and 7140 eV reflects the degree of plane distortion in the local environment of monatomic iron. Source data are provided as a Source data file.

corresponded to weak characteristic signals for $[FeC]^-$ and $[FeO]^-$, respectively. In contrast, pronounced signals for the fragment $[FeN]^-$ (m/z = 69.94) were observed, indicating the presence of only Fe–N bonds in Fe-SACs (Supplementary Fig. 8c). X-ray absorption spectroscopy (XAS) was employed to probe the chemical states and coordination environments of Fe-SACs. The Fe K-edge X-ray absorption near-edge structure (XANES) spectra demonstrated that the absorption edge intensities of Fe-SACs lie between those of FeO and Fe_2O_3, closely resembling iron phthalocyanine (FePc) (Fig. 1f). Quantitative analysis of XANES derivative spectra yielded average Fe valence states of +2.39 and +2.76 for Fe-CN and Fe-NCN, respectively, consistent with Fe 2p XPS results (Fig. 1f inset and Supplementary Fig. 8b). Compared to Fe-CN, Fe-NCN exhibited reduced pre-edge intensity and enhanced white-line intensity, indicative of decreased symmetry and charge redistribution in the coordination environment[23]. Fourier-transform extended X-ray absorption fine structure (FT-EXAFS) spectra showed a prominent Fe-N coordination peak at ~1.5 Å without metallic Fe–Fe bonds, confirming single-atom dispersion (Fig. 1g). This conclusion was further supported by wavelet transform (WT)-EXAFS analysis (Supplementary Fig. 9). Notably, the Fe-NCN primary peak exhibited a positive shift compared to Fe-CN and Fe foil, suggesting increased N coordination number ($n > 4$)[24]. EXAFS fitting on k-space and R-space revealed average Fe-N coordination numbers of 4.28 and 5.13 for Fe-CN and Fe-NCN, respectively (Supplementary Fig. 10 and Supplementary Table 2), which was also supported by TOF-SIMS analysis (Supplementary Fig. 8d). The comparable coordination environments between Fe-CN and FePc confirmed the planar $Fe\text{-}N_4$ configuration in Fe-CN. In contrast, the significantly higher planar distortion index ($I_A/I_B = 1.12$ vs. 0.98) observed in Fe-NCN compared to Fe-CN (Fig. 1h)[25], combined with excellent agreement between experimental data and simulated XANES spectra for the axial coordination model (Supplementary Fig. 11), conclusively demonstrated that isolated Fe atoms in Fe-NCN adopt a distorted square pyramidal configuration with four in-plane N atoms and one axial N ligand ($FeN_4\text{-}N_{axial}$).

Fenton-like catalytic reactions for pollutant removal

Typically, the oxidative removal of TCP via P-AOPs is challenging because the substitution of active hydrogens in the ortho and para sites of TCP by organochlorines prohibits the generation of critical phenoxy intermediates triggered by the proton-coupled electron transfer pathway; furthermore, the shielding of the Cl atoms blocks the active sites on TCP to proceed the polymerization reaction via conventional radical and ETP pathways[6,11]. In this work, PMS alone exhibited negligible TCP removal (Fig. 2a). In contrast, Fe-NCN achieved complete removal of TCP within 2.5 min, with its pseudo-first-order rate constant (k_{obs}) reaching 157, 59, and 17-fold higher than those of metal-free N-C (direct pyrolysis of the chelating agent), CN, and Fe-CN (Supplementary Fig. 12a). The adsorptive removal of TCP for Fe-NCN was only 2.4% within 10 min, indicating that TCP was removed through catalytic oxidation (Supplementary Fig. 12b). The iron leaching from Fe-NCN after reaction was approximately 7.02 μg/L, while Fe^{2+} at the same concentration only achieved 3.1% TCP removal with the presence of PMS, excluding the contribution of homogeneous reactions (Supplementary Fig. 12c).

The intrinsic catalytic activity was assessed using surface area-normalized rate constant (k_{SSA}), turnover frequency (TOF), and reaction parameter-normalized rate constant (k_{Nor}) (Fig. 2b and Supplementary Table 3). Obviously, Fe-NCN demonstrated overwhelming superiority over other materials across all these metrics. During cycling tests, the Fe-NCN/PMS system maintained high removal efficiency across six consecutive cycles with low iron leaching (Supplementary Fig. 12d). The Fe-NCN/PMS system also maintained superior TCP removal efficiency over a wide initial pH range of 1.0–9.0. However, when the pH was increased to 12.0, Fe-NCN exhibited a significantly inhibited removal efficiency, and this alkaline inhibition could be attributed to the electrostatic repulsion between the PMS anion and the hydroxylated and negatively charged catalyst surface[10] (Supplementary Fig. 13). Furthermore, intrinsic activity of Fe-NCN based on TOF and k_{Nor} surpassed state-of-the-art atomic and nanoparticle Fenton-like catalysts (Fig. 2c and Supplementary Tables 4 and 5).

Furthermore, Fe-NCN also demonstrated significantly enhanced oxidation efficiencies compared to Fe-CN for removing other micropollutants such as halogenated/dehalogenated phenolic compounds and sulfonamide compounds (Supplementary Fig. 14). Of particular interest, both Fe-NCN and Fe-CN exhibited slower removal kinetics toward electron-deficient organic pollutants, such as atrazine (ATZ), nitrobenzene (NB), and benzoic acid (BA), which are common radical probes, implying the selective non-radical nature of the two systems[26]. Such selectivity of non-radical oxidation can effectively mitigate interference from inorganic ions and organic humic substances in water matrices[24,27]. As shown in Supplementary Fig. 15, the presence of 10 mM inorganic anions showed a negligible impact on TCP removal. Even with 50 mg/L humic acid, TCP removal was inhibited by less than 10%. Additionally, Fe-NCN exhibited excellent TCP removal efficiency in tap water, surface water, and secondary effluent of wastewater treatment plants (Supplementary Fig. 16).

Acute toxicity was evaluated by calculating the relative inhibition of *P. phosphoreum* luminescence intensity before and after the reaction. The Fe-CN/PMS system showed rapidly increasing acute toxicity levels during the reaction, while the Fe-NCN/PMS system exhibited significantly reduced toxicity (Supplementary Fig. 17a). This observation strongly correlated with the dechlorination trends (Supplementary Fig. 17b), reflecting rapid TCP dechlorination into less/non-chlorinated products of low toxicity in the Fe-NCN/PMS system[28].

As shown in Supplementary Fig. 18a, although Fe-CN removed 64.1% of TCP within 10 min, only ~20% of total organic carbon (TOC) was eliminated in the bulk solution. In contrast, Fe-NCN achieved near-complete TOC removal (~98%). Chemical oxygen demand (COD) analysis after TCP removal revealed ~80% residual COD in bulk solution and ~7% COD remained on the catalyst in the Fe-CN/PMS system, whereas the Fe-NCN system retained <5% COD in bulk solution and ~93% on the catalyst (Fig. 2d and Supplementary Fig. 18b). These results collectively suggest the oxidative transformation of organic pollutants through a non-mineralization pathway in the Fe-NCN/PMS system with the polymeric products accumulated on the catalyst surface[6,10,29]. Thermogravimetric analysis (TGA) further confirmed this conclusion (Supplementary Fig. 19). In the Fe-NCN/PMS/TCP system, the theoretical maximum electron equivalents obtained by PMS (0.6 mM) were substantially lower than those provided for pollutant mineralization (2.12 mM), achieving an electron utilization efficiency of ~354% (Fig. 2e), while the electron utilization efficiency of the Fe-CN/PMS system was only 48.1% (Supplementary Table 6). These results imply the distinct pollutant transformation pathways in Fe-CN and Fe-NCN-based systems.

Reaction pathway regulation by axial coordination

Quenching experiments and electron paramagnetic resonance (EPR) spectroscopy were employed to identify potential ROS in catalytic systems. As shown in Supplementary Fig. 20, excess scavengers, including methanol (MeOH), tert-butanol (TBA) and isopropanol (IPA), exhibited negligible inhibitory effects in the Fe-SACs/PMS system, eliminating the contribution of hydroxyl radicals ($^{\bullet}OH$) and sulfate radicals ($SO_4^{\bullet-}$) as primary oxidative species[27,30]. The absence of radical species was further corroborated by radical trapping and chemical probing tests with EPR and photoluminescence detection (Supplementary Figs. 21 and 22). Additionally, both the absence of a featured bisguanidine product in the chemical tests probed with nitroblue tetrazolium (NBT) and the negligible TCP removal in the O_2 atmosphere ruled out the oxidative contribution of superoxide radicals ($O_2^{\bullet-}$)

https://doi.org/10.1038/s41467-026-69253-y

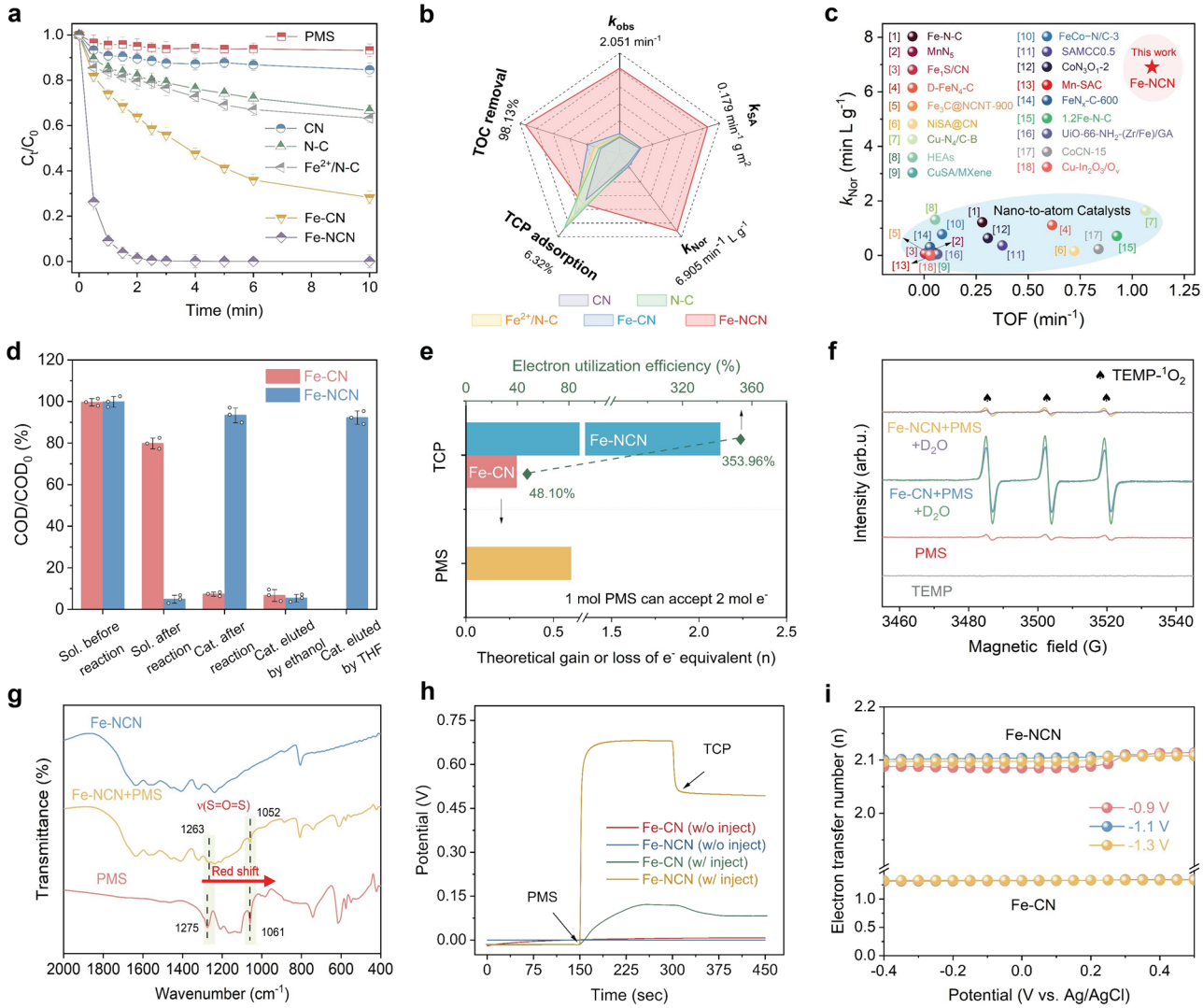

Fig. 2 | Catalytic activity of catalyst and identification of oxidation mechanisms. a Removal of TCP by different catalysts/PMS systems. Data are presented as mean values ± s.d. (n = 3). **b** A critical evaluation of Fe-SACs/PMS in different aspects. **c** Intrinsic catalytic activity of the Fe-NCN in comparison with the state-of-the-art SACs and metal-based material in PMS-based Fenton-like oxidation. The comparative data points (annotated [1]–[18]) are taken from the literature cited in the Supplementary Information, corresponding to Supplementary Refs. 21–38. **d** Residual COD of the reaction solution and of the reacted Fe-SACs after elution with different solvents. **e** Electronic utilization efficiency of Fe-SACs/PMS/TCP system. Experimental condition: $[\text{pollutant}]_0$ = 0.1 mM, $[\text{PMS}]_0$ = 0.3 mM, [catalyst] = 0.1 g L^{-1}, $[\text{pH}]_0$ = 6.7, initial T = 25 °C. Data are presented as mean values ± s.d. (n = 3). **f** EPR spectra of TEMP adducts recorded during PMS activation in Fe-SACs systems. **g** In situ FTIR spectra of Fe-NCN system. The signal peaks in the green shaded area represent the O=S=O groups in PMS. **h** OCP changes upon sequential addition of PMS and TCP for Fe-SACs electrodes. Experimental condition: $[\text{PMS}]_0$ = 5.0 mM, [catalyst] = 0.4 g, $[\text{pH}]_0$ = 6.7, initial T = 25 °C. **i** The number of electron transfers fitted by the rotating ring disc electrode (RRDE) experiment. Source data are provided as a Source data file.

(Supplementary Fig. 23)[24]. These findings conclusively validate the non-radical oxidation pathways in the Fe-SACs/PMS system.

High-valent metal-oxo species, singlet oxygen ($^1O_2$), and surface-bound PMS complexes (PMS*) are widely recognized as typical non-radical reactive species in Fenton-like catalysis[30–32]. However, dimethyl sulfoxide (DMSO) quenching experiments and methyl phenyl sulfoxide (PMSO) probing revealed no presence of high-valent Fe-oxo intermediates in the Fe-SACs/PMS system (Supplementary Fig. 24). Since the intermetallic Fe-O species can exchange an oxygen atom with water, we further applied ^{18}O isotope labeling experiments to exclude the presence of high-valent Fe-oxo intermediates[33]. If Fe-oxo species exist in the system, their isotopic oxygen exchange with $H_2{}^{18}O$ results in the formation of ^{18}O-containing Fe-oxo species, and such labeled Fe-oxo species can transfer ^{18}O to the coexisting PMSO to generate detectable $PMSO^{18}O$. However, when the reaction system was transferred to the $H_2{}^{18}O$ matrix, the two characteristic peaks of $PMS^{16}O^{16}O$ (m/z = 157) and $PMS^{16}O^{18}O$ (m/z = 159) were hardly detected, and the two characteristic fragments of $PMS^{16}O^{18}O$ with two mass unit deviations were not observed in the MS^2 spectra.

Furfuryl alcohol (FFA) and 2,2,6,6-tetramethyl-4-piperidinol (TEMP), as single-linear oxygen ($^1O_2$) scavengers, severely inhibited pollutant removal after addition to the Fe-CN/PMS system (Supplementary Fig. 20). Furthermore, EPR test using TEMP as the $^1O_2$ probe revealed apparent triplet signals for $^1O_2$ which was augmented in D_2O, further supporting that $^1O_2$ was generated in this system (Fig. 2f and Supplementary Fig. 25)[8,34]. Trace amounts of FFA were used as competitive kinetic probes to further evidence the dominant contribution of $^1O_2$ to TCP oxidation in Fe-CN/PMS (86.9%) (Supplementary Fig. 26). In contrast, the Fe-NCN/PMS system exhibited negligible $^1O_2$ signals, indicating alternative non-radical pathways. No significant fluorescence signal was detected in Fe-NCN/PMS system after the addition of singlet oxygen sensor green (SOSG), further excluding $^1O_2$ generation

(Supplementary Fig. 27)[35]. These findings collectively demonstrate that 1O2 is the primary reactive species in Fe-SACs/PMS, whereas it was not produced in the Fe-NCN/PMS system.

To probe the formation of surface PMS* complex to coordinate a non-radical ETP regime for TCP removal, the interaction between Fe-NCN and PMS was investigated using in situ Fourier transform infrared spectroscopy (IS-FTIR) (Fig. 2g). Upon introducing Fe-NCN, the stretching vibration peaks corresponding to HSO_5^- (1061 cm^{-1}) and SO_4^{2-} (1275 cm^{-1}) shifted to 1052 cm^{-1} and 1263 cm^{-1}, respectively, with marked attenuation in peak intensity. This shift corresponds to reduced electron density in S=O bonds, confirming the formation of metastable PMS* complexes[36]. In contrast, no such peak shifts were observed in $^1O_2$-based Fe-CN/PMS system (Supplementary Fig. 28). Similarly, in situ Raman spectroscopy (IS-Raman) detected a transient PMS-associated peak at ~831 cm^{-1} upon PMS addition, which disappeared following TCP introduction, mirroring PMS complex (PMS*) formation and consumption dynamics (Supplementary Fig. 29)[37]. The reactivity of pre-oxidized catalyst by PMS and post-oxidation-reaction catalyst was also assessed (Supplementary Fig. 30)[38]. Pre-oxidized Fe-NCN (stored in PMS solution for 3 h) rapidly removed ~93% of TCP within 1 min, while the reacted catalysts still retained ~26% TCP removal, indicating the formation of long-lived PMS* intermediates on Fe-NCN surface that contributed to TCP oxidation via a non-radical manner. The PMS consumption profile in Fe-NCN systems exhibited strong pollutant dependence, with PMS decomposition increasing drastically after TCP addition, as evidenced by the ETP mechanism (Supplementary Fig. 31). This is different from the Fe-CN system, where the presence of the pollutant did not affect PMS consumption, as PMS was continuously decomposed into $^1O_2$[29,39].

As expected, the open loop potential (OCP) and timing currents of Fe-NCN showed sharp changes in response to PMS and TCP addition (Fig. 2h and Supplementary Fig. 32a)[40], but no significant changes were found in Fe-CN. Linear voltammetry curves (LSV) showed that the positive current density of the Fe-NCN electrode was significantly increased in the presence of PMS, confirming that the continuous electron transfer from the catalyst to PMS (Supplementary Fig. 33)[27]. Conversely, Fe-CN exhibited a predominant cathodic current at negative potentials, suggesting that electrons tend to transfer from PMS to Fe-CN[41]. This process can trigger the dissociation of O–H bond, thereby resulting in the formation of persulfate radicals ($SO_5^{\bullet-}$) that serve as a critical precursor for $^1O_2$ formation ($2SO_5^{\bullet-} + 2e^- \rightarrow 2SO_4^{2-} + {}^1O_2$). Furthermore, rotating ring-disk electrode (RRDE) measurements confirmed the dual-electron transfer process during TCP oxidation via ETP in Fe-NCN/PMS, in contrast with one-electron transfer for Fe-CN to mediate $SO_5^{\bullet-}$ (Fig. 2i and Supplementary Fig. 34)[42]. Collectively, Fe-NCN with axial N coordination triggers the PMS activation pathway, transitioning from $^1O_2$ generation (FeN_4, Fe-CN) to ETP (FeN_4-N_{axial}, Fe-NCN) in Fe-SACs/PMS.

Theoretical revelation of oxidation mechanisms

In the ETP pathway, contaminants can be oxidized either by PMS* via direct inner/outer-shell interactions (denoted as short-range ETP, featured as point oxidation) or indirectly through the conductive catalysts that act as an electron shuttle (denoted as long-range ETP, featured as domain-based/anode-like oxidation) (Fig. 3a)[6,43]. Three customized reactor configurations elucidated these pathways in the Fe-NCN/PMS/TCP system (Fig. 3c and Supplementary Text 16). In the dual-chamber reactor (Mod. 1) with separated TCP and PMS, the Fe-NCN electrode showed low transient current (~21 μA) and limited TCP removal efficiency (~17%) (Supplementary Fig. 35a). The electrode plate-separated dual-chamber reactor (Mod. 2) showed marginally improved removal efficiency (~22%) when PMS and pollutant are separated, while the single-chamber reactor (Mod. 3) achieved rapid and complete TCP elimination within 2.5 min (Supplementary Fig. 35b). The significant difference between the different reactors demonstrated that the necessity of concurrent presence of PMS and Fe-NCN, suggesting the direct oxidation feature of short-range ETP in the Fe-NCN/PMS system (Fig. 3d). This pathway was enabled by the direct inner-sphere interactions of pollutant and surface activated PMS*, as evidenced by its great immunity to $NaClO_4$ interference (Supplementary Fig. 20)[28,43].

Indeed, the semiconducting properties of CN, with its limited charge-transfer capacity, disabled the substrate as an electron shuttle to mediate charge transfer from the contaminant to surface-activated PMS, leading to short-range ETP-dominated contaminant oxidation (Supplementary Figs. 32b and 36)[42]. In contrast, the highly graphitic and conductive carbon nanotube (CNT) electrode exhibited a significant transient current (~194 μA) and achieved ~73% TCP removal in the galvanic cell, suggesting the long-range ETP dominated oxidation (Supplementary Fig. 37). However, the CNT/PMS system exhibited a low dechlorination efficiency (~4%), with predominant products as polychlorinated biphenyl compounds that typically exhibit higher toxicity than the parent TCP (Supplementary Fig. 38). DFT calculations elucidated the different dechlorination behaviors of the short-range and long-range ETPs for TCP removal (Supplementary Fig. 39). When the distance between TCP and CNT/PMS* was between 10 and 20 nm, the C–Cl bond can be hardly activated. However, when the distance decreases to 2–10 nm, the interfacial electron transfer between the aromatic π system of TCP and the electrophilic complex PMS* is significantly enhanced. This intensifies the shift of the electron density on the C–Cl bond towards the chlorine atom, resulting in the weakening and elongation of the C–Cl bond (1.72 → 1.75 Å). These findings emphasized that close spatial matching between PMS* and pollutants is a crucial factor in regulating C–Cl bond cleavage over catalysts (Fig. 3b).

Remarkably, regulating in-plane coordination number from FeN_4 to FeN_{4+1} slightly enhanced PMS adsorption energy (E_{ads} = −3.96 vs. −4.02 eV) and electron transfer (−0.88 e vs. −0.91 e) (Supplementary Fig. 40). However, although axial N coordination significantly reduced E_{ads} to −2.98 eV with moderated electron transfer (−0.85 e), it favored metastable low-spin Fe-PMS* complex formation (Fig. 3e, Supplementary Figs. 41 and 42 and Supplementary Table 7). The projected crystal orbital Hamilton population (pCOHP) analyzed the bond strength between the central Fe atom and the O atom of the O–O bond during PMS activation. Axial coordination lifted the antibonding orbitals and decreased the electronic occupancy in these regions, leading to significantly increased IpCOHP for the Fe–O bond (−1.10 → −1.83 eV), which facilitated the formation of more stable PMS* intermediates (Fig. 3f). After adsorption of PMS, the center of the *d* band of Fe-NCN was closer to the Fermi energy level than that of Fe-CN (−2.07 eV vs. −2.28 eV), indicating that axial N coordination broadens the d-electronic energy level distribution of the central Fe atoms and promote its interactions with PMS to coordinate an electron transfer process (Fig. 3e and Supplementary Fig. 43)[44].

Temperature-dependent magnetization measurements, EPR tests and spin-orbit filling calculations further determined the spin state of the Fe atom (Supplementary Figs. 44–47 and Supplementary Table 8)[45]. The lower ratio of spin states to unpaired electrons in Fe-NCN compared to Fe-CN suggests that the axial ligand exerts an electron-pulling effect on the Fe site by manipulating the spin electrons. Specifically, due to the geometrical distortion ($D_4h \rightarrow C_3v$) induced by the axial coordination configuration, the simplified d_{xz} and d_{yz} orbitals of Fe-NCN split into non-simplified orbitals, leading to a staggered energy rearrangement of the $d_{x^2-y^2}$ and d_{z^2} orbitals, and consequently to decreased unpaired electrons in e_g orbitals, giving rise to the low spin state[46] (Fig. 3g). The change in orbital configuration and the reduction of half-filled orbitals of Fe-NCN promote the charge transfer from e_g orbital centers the Fe site to PMS molecules to form PMS* intermediates to initiate ETP (Supplementary Fig. 48). In

https://doi.org/10.1038/s41467-026-69253-y

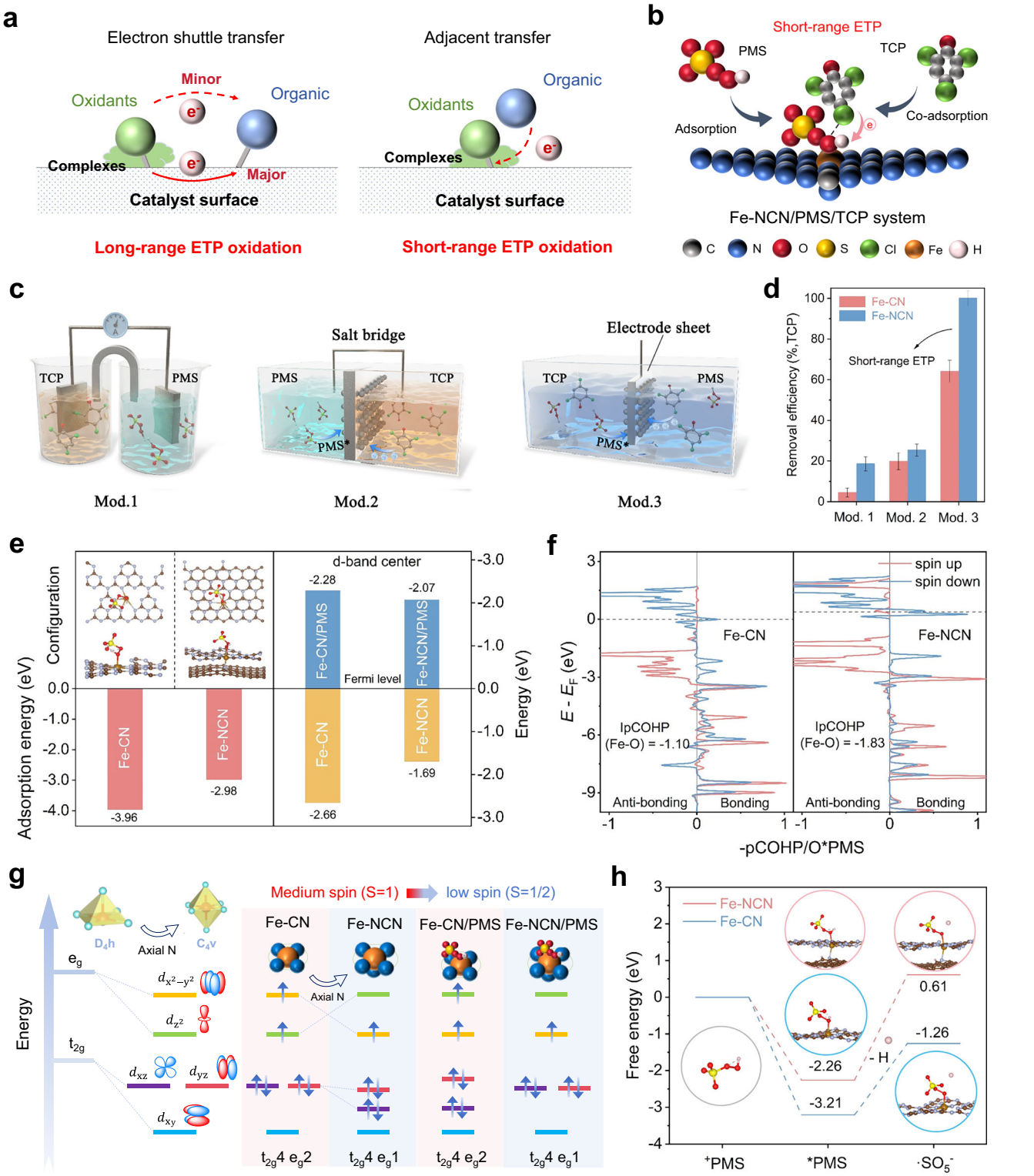

Fig. 3 | Mechanistic investigation of axial ligand-induced catalytic pathway transitions. a Schematic diagrams of the two different ETP paths. **b** Short-range ETP mechanism of oxidized pollutants in Fe-NCN/PMS system. **c** Three different galvanic model reactors. **d** Performance of TCP removal by Fe-SACs activated PMS in three model reactors. Experimental condition: $[\text{pollutant}]_0 = 0.1$ mM, $[\text{PMS}]_0 = 0.5$ mM, [catalyst coat] = 0.5 mg cm^{-2}. Data are presented as mean values ± s.d. (n = 2). **e** The adsorption configuration, adsorption energy of Fe-SACs/PMS and the d band center of catalyst before and after PMS adsorption. **f** pCOHP between the Fe atom and the O atom as PMS adsorption. Corresponding IpCOHP values are shown in the figures. **g** Spin states of Fe-CN (Fe-N_4), Fe-NCN (Fe-$N_{4+axial}$), Fe-CN/PMS, and Fe-NCN/PMS. **h** Pathways and corresponding thermodynamic change curves of $^1O_2$ generation from PMS activated by Fe-SACs. The crystal structures in **e** and **h** are constructed with VESTA software[62]. Source data are provided as a Source data file.

contrast, the mid-spin state of Fe-CN underwent strong coordination and local transfer of unpaired electrons with PMS, resulting in significantly stretched O–H bond in PMS (0.98 Å → 1.03 Å), leading to a low-energy barrier for deprotonation to produce $SO_5^{\bullet-}$, two of which subsequently dismutate into $^1O_2$ (Fig. 3h and Supplementary Table 7). Compared to Fe-NCN, Fe-CN only required overcoming a lower reaction energy barrier (1.95 vs. 2.87 eV) to achieve dissociation of the high-bond-energy O–H bond, thereby driving the entire process into a thermodynamically favorable state (ΔG = −1.26 eV). As expected, the energy difference of charge transfer from the e_g center in Fe-CN to the PMS increases significantly, reversing the direction of electron transfer from PMS to the catalyst, yielding $SO_5^{\bullet-}$.

Steered polymerization reaction mechanism

To elucidate the short-range ETP-driven contaminant polymerization mechanism, we systematically examined the compositional change of the catalyst before and after reactions. XPS and FTIR spectra revealed intensified C–O–C (1065 cm^{-1}), C–C (1582 cm^{-1}), and C–O (1237 cm^{-1}) vibrational modes on reacted Fe-NCN, indicating substantial polyphenyl ether accumulation (Fig. 4a and Supplementary Figs. 49 and 50). Subsequently, the possible small molecule products (~14%) and large molecule products (~83%) were eluted by stepwise solubilization using ethanol and tetrahydrofuran (THF) in sequence, and the eluates appeared as clear and yellowish-brown colors, respectively (Supplementary Fig. 51). The ethanol-eluted small molecule products were analyzed using high-performance liquid chromatography-mass spectrometry (HPLC-MS) testing and identified as the C-C coupled products (i.e. Biphenyl-2,2′,5,5′-tetrol (m/z = 217)). Structural analysis of the THF-eluted solubilised products by nuclear magnetic resonance (NMR), gel permeation chromatography (GPC) and matrix-assisted laser desorption/ionization time-of-flight mass spectrometry (MALDI-TOF-MS) identified the macromolecular products as crosslinked polyphenylene ethers formed mainly via C-O linkage, with an average molecular weight (Mn) of 4292 Da (Supplementary Figs. 52–56)[6,10]. Notably, more products were collected using THF as the eluent than with toluene, suggesting that the products may be predominantly polar, medium-molecular-weight oligomers (Supplementary Fig. 57a).

Remarkably, most of the macropolymers did not retain organochlorines, coinciding with the rapid and complete dechlorination of the system (Supplementary Fig. 17b), accompanied by the formation of many phenolic hydroxyl groups. IS-Raman spectroscopy directly confirmed hydroxyl substitution of aromatic chlorine during TCP polymerization, as evidenced by time-dependent intensification of the Fe–OH stretching vibration at 578 cm^{-1} and concomitant attenuation of the C–Cl bond signal at 667 cm^{-1} (Fig. 4b)[47,48]. This process was also confirmed by the increased content of hydroxyl groups on the catalyst surface (Supplementary Fig. 57b–d).

Based on these results, we further investigated the key intermediates for TCP polymerization transfer in the catalytic system. The inner-sphere nature of short-range ETP precludes outer-sphere single-electron abstraction from TCP by PMS* to form chlorophenoxyl radical cations ($TCP^{\bullet+}$)[7]. The inner-sphere oxidation pathway between the surface complex PMS* and the substrate was identified using 3-ethylbenzothiazoline-6-sulfonic acid (ABTS) as a probe compound. Component quantification calculations showed that ABTS was rapidly oxidized to the green persistent radical of $ABTS^{\bullet+}$ in the Fe-CN/PMS system (Supplementary Fig. 58), featured by the four characteristic absorption peaks at 415, 643, 728, and 818 nm (Supplementary Fig. 59), via either the single electron transfer (SET) or hydrogen atom abstraction (HAA) pathway[28,39]. This is consistent with the singlet oxygenation regime, in which, because of the unoccupied π* orbital, $^1O_2$ can attack and reduce electron-rich organic compounds via SET[49].

In contrast, Fe-NCN/PMS systems generated $ABTS^{2+}$ species with distinct absorption signatures at 216 and 293 nm[50], evidencing dual-electron transfer processes from ABST to PMS*. For deuterated phenol (C_6H_5OD), where the BDE of the O–D bond is distinctly higher than that of the O–H bond, the HAA pathway with phenolic hydroxyl groups as reaction sites is expected to lead to a significantly large KIE value[28]. However, insignificant kinetic isotope effects (KIE = 1.32) in Fe-NCN/PMS systems using C_6H_5OD as the substrate ruled out the HAA pathway as the dominant reaction pathway (Supplementary Fig. 60). The reaction system with D_2O as the solvent showed a primary KIE, which reached a value of 1.71 (the isotope effect is usually considered to play a dominant influence on the reaction rate when the KIE > 1.5)[51]. This result suggests that the cleavage/formation of C–H bonds plays a crucial role in the reactions, while the C atoms on the aromatic ring undergo a transition from sp^3 hybridization to sp^2 hybridization, providing strong evidence for the presence of metastable carbocationic intermediates during the reaction (Supplementary Fig. 25)[6,52]. Thus, the generation of chlorophenoxy radicals with varied resonance states ($TCP\text{-}(O)^{\bullet}$) was ruled out, which is the typical polymerization intermediate generated from SET via inner-sphere interactions[7].

Reference experiments with ferulic acid (FA, phenyl radical-specific probe) and EPR analyzes of DMPO as the spin trap did not show inhibitory effects, and characteristic signals in the quintuple state (1:4:6:4:1) further support the absence of the $TCP\text{-}(O)^{\bullet}$ intermediates (Supplementary Fig. 61)[7,53]. Subsequent trapping experiments with acetonitrile as a nucleophilic scavenger identified chlorophenoxonium ions ($TCP\text{-}(O)^+$) as crucial intermediates generated via two-electron transfer from TCP to metastable Fe-NCN/PMS* complex (Supplementary Fig. 62)[54]. The reactive $TCP\text{-}(O)^+$ intermediates further underwent C-C coupling to form dimers or C-O polymerization to yield oligomers through nucleophilic aromatic substitution.

To further unravel the PMS*-mediated DHP path activated by Fe-NCN, combined DFT calculations and molecular dynamics (MD) simulations were conducted. Initial, the axial ligand makes the adsorption of Fe-SACs/PMS* with para-chlorine in the TCP molecule significantly stronger than phenolic hydroxyls, providing the feasibility of C-Cl bond dissociation for the dual-electron transfer process (Supplementary Fig. 63). Based on this favorable conformation, the inner-sphere double electron transfer between TCP and the catalyst surface complex PMS* induces deprotonation of the phenolic hydroxyl group to form a chlorophenoxonium ion intermediate ($TCP\text{-}(O)^+$) as well as a pronounced stretching of the C–Cl bond (1.72 Å → 1.74 Å) with an exothermic release of −1.18 eV (IV′) or −1.97 eV (IV) (Fig. 4c, Supplementary Fig. 64 and Supplementary Table 9). While transient resonance delocalization may stabilize $TCP\text{-}(O)^+$ on catalytic surfaces, generating meta-carbocationic centers through aromatic polarization, the synergistic steric-electronic constraints imposed by chlorine substituents render these stabilized chlorophenoxonium ions kinetically inert toward subsequent coupling or polymerization pathways[55,56]. Since the bulk solution is weakly acidic, $TCP\text{-}(O)^+$ is rapidly protonated to $TCP\text{-}(OH_2)^+$. Note that the electronic effects and spatial site resistance of the $TCP\text{-}(OH_2)^+$ molecule, the C4 site tended to be preferentially attacked by nucleophilic OH^- (Supplementary Fig. 65, Fuki index f^+ = 0.015), which led to the substitution of para-chlorine (SNAr mechanism), giving rise to 2,6-dichlorobenzene diphenol ($OH\text{-}DCP\text{-}(OH_2)^+$, m/z = 178) (Supplementary Figs 66–68). The newly formed phenolic hydroxyl group donated electrons to the aromatic ring via a conjugated molecular network, stabilizing the radical intermediate. To validate the origin of the para-chloro-substituted hydroxyl atom, isotopic tracer experiments were conducted using $H_2{}^{18}O$, revealing that the hydroxyl oxygen of $OH\text{-}DCP\text{-}(OH_2)^+$ does not originate from PMS but water, as evidenced by LC-MS analysis (Supplementary Fig. 69). As the rate-determining step, water-induced hydroxylation of the cation intermediate experienced a much lower energy barrier than the direct substitution of para-chlorine with OH^{-*} (1.04 vs. 2.03 eV).

https://doi.org/10.1038/s41467-026-69253-y

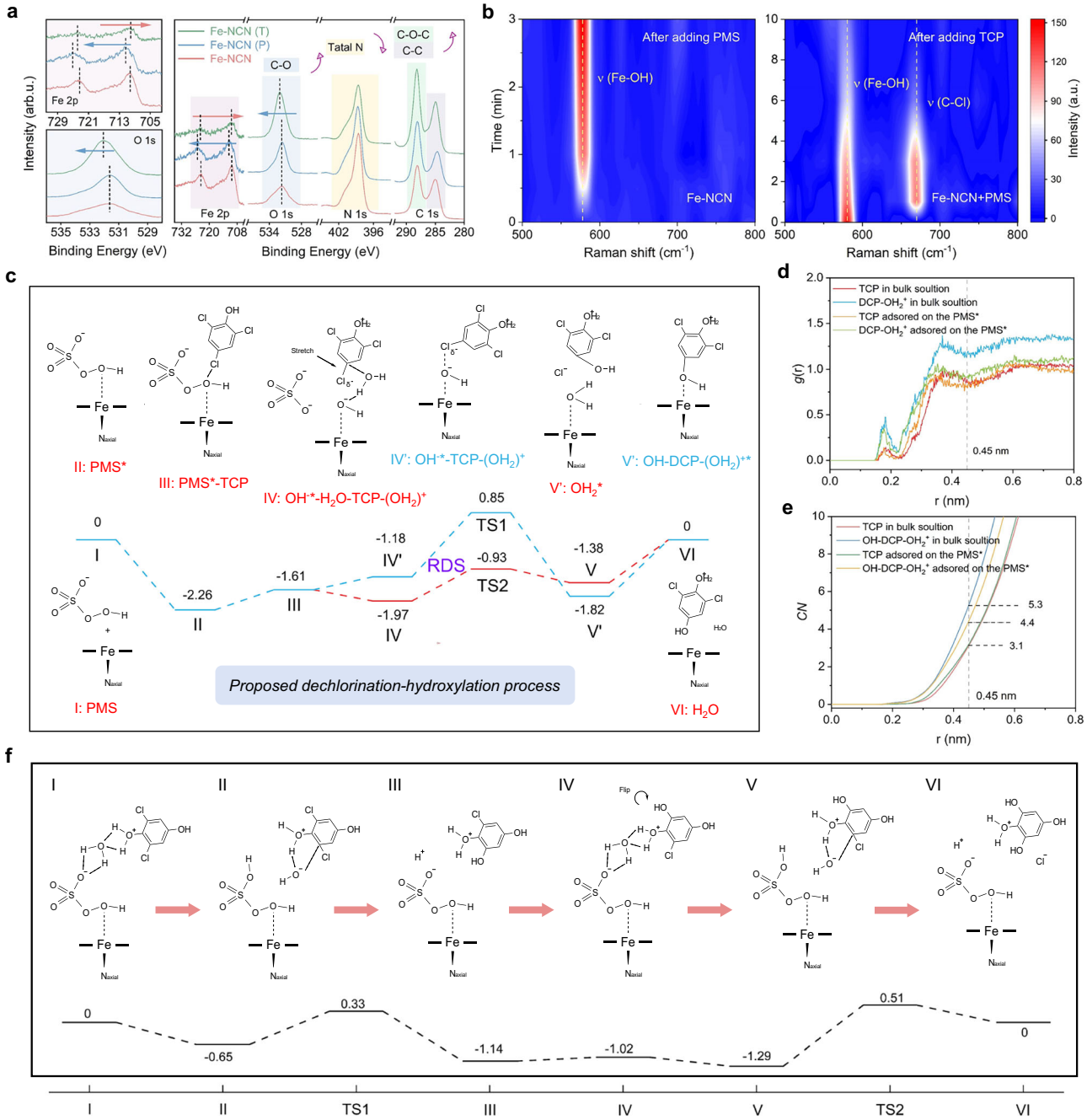

Fig. 4 | Identification of polymerization products and mechanism of C-O polymerization of pollutants in DHP path. a XPS spectra of Fe-NCN in the original, after activation of PMS, and after reaction with TCP. **b** Chemical evolution of the Fe-NCN surface based on in situ Raman spectra after sequential addition of PMS and TCP. Experimental condition: $[PMS]_0 = 5.0$ mM, [catalyst] = 0.5 g, [TCP] = 0.5 mM, $[pH]_0 = 6.7$, initial $T = 25$ °C. **c** Thermodynamic potential energy (Unit: eV) curve of hydroxylation-dechlorine reaction path based on short-range ETP induced by axial ligands. **d** Radial distribution function $g(r)$ for the organic molecule–O_w distance between organic molecule and the O atom of water. **e** Coordination number (*CN*) of water. **f** Synergistic modulation of hydroxylation substitution reaction pathways and thermodynamic potential energy (Unit: eV) profiles of ortho-chlorine on chlorophenoxonium ions by the electrophilic intermediate PMS* and water bridges. Source data are provided as a Source data file.

MD simulations indicate that OH-DCP-$(OH_2)^+$ has a tighter hydrogen bonding network and a larger diffusion coefficient compared to TCP, which facilitates its adsorption and stabilization with the terminal oxygen atoms of PMS* via a stable water bridge, releasing energy of 0.65 eV (Fig. 4d–f and Supplementary Figs. 70 and 71). Notably, this stable hydrogen bonding network effectively stabilized OH-DCP-$(OH_2)^+$, preventing the π-electron delocalization and resonance stabilization of radicals/ions required for quinone formation (Supplementary Fig. 72). Subsequently, under the charge-induced effect of the terminal oxygen atom, PMS* will release energy of 1.47 eV to capture a proton from H_2O after overcoming an energy barrier of 0.98 eV. The deprotonated H_2O will then undergo a low-energy barrier (0.12 eV) for nucleophilic attack on the ortho-chlorine, leading to spontaneous dehalogenation and hydroxylation. This mechanism of synergistically induced hydroxyl substitution of o-chloro on halogenated phenols by electrophilic intermediates and water bridges has also been similarly reported in dehalogenated peroxidases[18]. After undergoing a further hydroxylation process in a similar manner, TCP

was finally completely dehalogenated, yielding the more stable trihydroxyphenoxonium ion (Supplementary Figs. 73 and 74). Subsequently, these electron-rich and stable phenoxyeonium ion intermediates were readily linked via the phenolic hydroxyl groups of another (chloro)phenols, leading to spontaneous C-O polymerization.

Practical application investigation

To evaluate the applicability of Fe-NCN for real wastewater treatment, understanding the impact of oligomer accumulation on catalytic stability is critical. Previous studies have demonstrated that polymeric products' adhesion and accumulation on catalyst surfaces induce self-inhibitory effects, leading to rapid catalytic deactivation[14,57]. Organic solvent elution effectively removed the adsorbed oligomers on the catalyst surface, refreshing "deactivated" catalysts with 98.3% of the initial activity (Fig. 2d and Supplementary Fig. 75). To understand the competition between oligomers and reactants, 4,4′-bisphenol was used as a competing probe for polymerization reactions (Supplementary Fig. 77a), as 4,4′-bisphenol is a potential coupling product with similar hydrophobicity to TCP but has a higher polarity and highest occupied molecular orbital (HOMO, more susceptible to oxidation).

As shown in Supplementary Fig. 76, the Fe-NCN/PMS system maintained TCP removal efficiency when 4,4′-bisphenol was added, while the Fe-CN/PMS system exhibited a loss of 40% activity. Comparative adsorption analyzes (Supplementary Fig. 77b) showed that the adsorption capacity of the materials exhibits a strong positive correlation with the surface zeta potential and hydrophobicity. The higher zero-charge point favors the specific adsorption of oligomers with polar functional groups by polarity matching (Supplementary Fig. 77c). In addition, enhanced hydrophobicity promotes interactions between the substrate and the hydrophobic structure of the oligomer, reducing the competition of the product for the active site (Supplementary Fig. 77d). Indeed, this is primarily attributed to the introduction of the chelator 1,10-phenanthroline, whose pyrolytic formation of N-C confers a hydrophobic and polar microenvironment in the vicinity of the active centers in Fe-NCN. This hydrophobic/polar microenvironment extensively exists in the binding pocket of natural enzymes, which is a key prerequisite for specific catalysis and efficient cycling[18,20,58] (Fig. 1a and Supplementary Fig. 2). Therefore, mimicking the enzyme hydrophobic/polar binding pocket microenvironment can effectively retard the product coverage of the active site based on the DHP path to maintain the catalytic stability of the atomic catalyst.

Bleached wastewater collected from the pulp and paper industry was used to evaluate the practicality of the Fe-NCN/PMS system. The results showed that the catalyst performed well in treating the actual wastewater, removing more than 85.7% of COD (Fig. 5a). The excitation emission matrix (EEM) spectra showed a significant reduction in the fluorescence intensity of the solution after the reaction, suggesting that organics such as microbial by-products in the wastewater samples were readily removed (Fig. 5b).

We further assessed Fe-NCN for practical applications at the device level. A membrane-catalyzed microreactor was employed to evaluate the long-term stability of DHP technology by continuously treating simulated wastewater. As shown in Supplementary Fig. 78, the catalyst coating of Fe-NCN (20 mg) was uniformly covered on the microfiltration membrane, which could effectively remediate 6 L of TCP wastewater (2.0 ppm) at a flow rate of 0.5 L/h. TOC removal and dechlorination were maintained above 80% and 90%, respectively, and the leaching of Fe ions was very low (<7 μg/L). The DHP-based technology is further scaled up using a larger fluid-bed reactor configuration embedded with the Fe-NCN catalyst. The river stones with an average size of 10–20 mesh were used to fix 5.0 g of catalyst in the reaction layer, and the inlet and outlet ports were isolated by quartzite to form an enlarged reaction unit (Fig. 5c). The fluidized bed reactor was still able to achieve close to ~100% TCP removal, above 80% TOC removal and 90% dechlorination over 60 days (2 mL/min flow rate), equivalent to 34.56 L/g purification capacity (Fig. 5d). Given these results, a tonne of TCP wastewater can be treated at the expense of $USD 0.37 (Supplementary Table 10).

The post-reaction catalysts were regenerated via ethanol/THF elution washing and to recover organic solid products (Fig. 5e and Supplementary Fig. 79). By adding a methanol-water mixture to the THF solution, a powdery product was precipitated, taking advantage of the difference in solubility. Uniformly sized plastic pellets were obtained by the extrusion-condensation-granulation process after drying treatment (Fig. 5f). The excellent and stable properties of these pellets, which are mainly composed of phenolic hydroxyl carbon and ether-bonded aromatic rings (Fig. 5g), allow further injection and molded into a wide range of high-performance plastic products with great potential for real-world applications (Supplementary Text 20, Supplementary Fig. 80 and Supplementary Table 11).

Besides the excellent performance of the material, the potential for scale-up synthesis is also one of the most important concerns in practical applications. Thus, we conducted TEA and LCA evaluations to assess the economic-environmental feasibility of the per-tonne scale-up process. The results show that the plant-gate levelized cost per tonne of Fe-NCN macroscale, based on our synthesis method, is projected to be lower than the current market prices of activated carbon and cobalt oxide (Fig. 5h), which serve as representative adsorbents and P-AOP catalysts, respectively[6]. Once optimized chemical input ratios, the cost could be further reduced in the future (Supplementary Text 21 and Supplementary Tables 12–14)[57]. Considering further the profitability of polymer recycling, the cost decreased significantly by 31.9% to US$ 6739.79 (Supplementary Text 22). Crucially, the quantitative LCA results for the scaled-up synthesis of Fe-NCN and Fenton-like performance demonstrated significantly lower environmental impacts compared to typical mineralization-based AOP catalysts (i.e., zeolite azolium salt framework-based iron monoatom and commercial nano zero-valent iron) across both material synthesis and treatment processes (Supplementary Fig. 81 and Supplementary Tables 15 and 16)[24,59]. The product recovery step after the polymerization process reduced the global warming potential (GWP) of the Fe-NCN/PMS system by ~78%, indicating a substantially decreased carbon footprint. Overall, these results suggested that Fe-NCN is suitable for industrialization with excellent long-term stability, lower production cost, and significantly reduced environmental impacts.

Discussion

In this work, we engineered a controlled dehalogenation-coupled directional polymerization pathway for HOPs, achieving enhanced polymerization efficiency while suppressing toxic halogen release. Inspired by the enzyme structure, the precisely constructed Fe-NCN, with well-defined axial N-coordinated FeN_4 sites, triggered a transition in the TCP oxidation pathway from singlet oxygenation to short-range ETP. Fe-NCN mediated dual-electron transfer from TCP to the activated electrophilic PMS* intermediates, inducing O–O bond cleavage to generate featured nucleophilic OH^{-*} species that drive para-chlorine nucleophilic substitution. Furthermore, surface PMS* mediates the nucleophilic substitution of o-chlorophenoxidinium ions through water-bridged pathways, resembling the distinctive dehalogenation and hydroxylation mechanisms of dehaloperoxidases in nature. Notably, this dehalogenation process constructs additional polymerization sites on TCP by providing additional phenolic hydroxyl groups on benzene rings for subsequent C-O polymerization. This nucleophilic-electrophilic sequential coupling reaction pathway enables TCP not only to undergo dechlorination and detoxification but also to accelerate polymerization reactions by creating carbocation sites via transient resonance transfer and by generating phenolic hydroxyl groups via hydroxylation.

https://doi.org/10.1038/s41467-026-69253-y

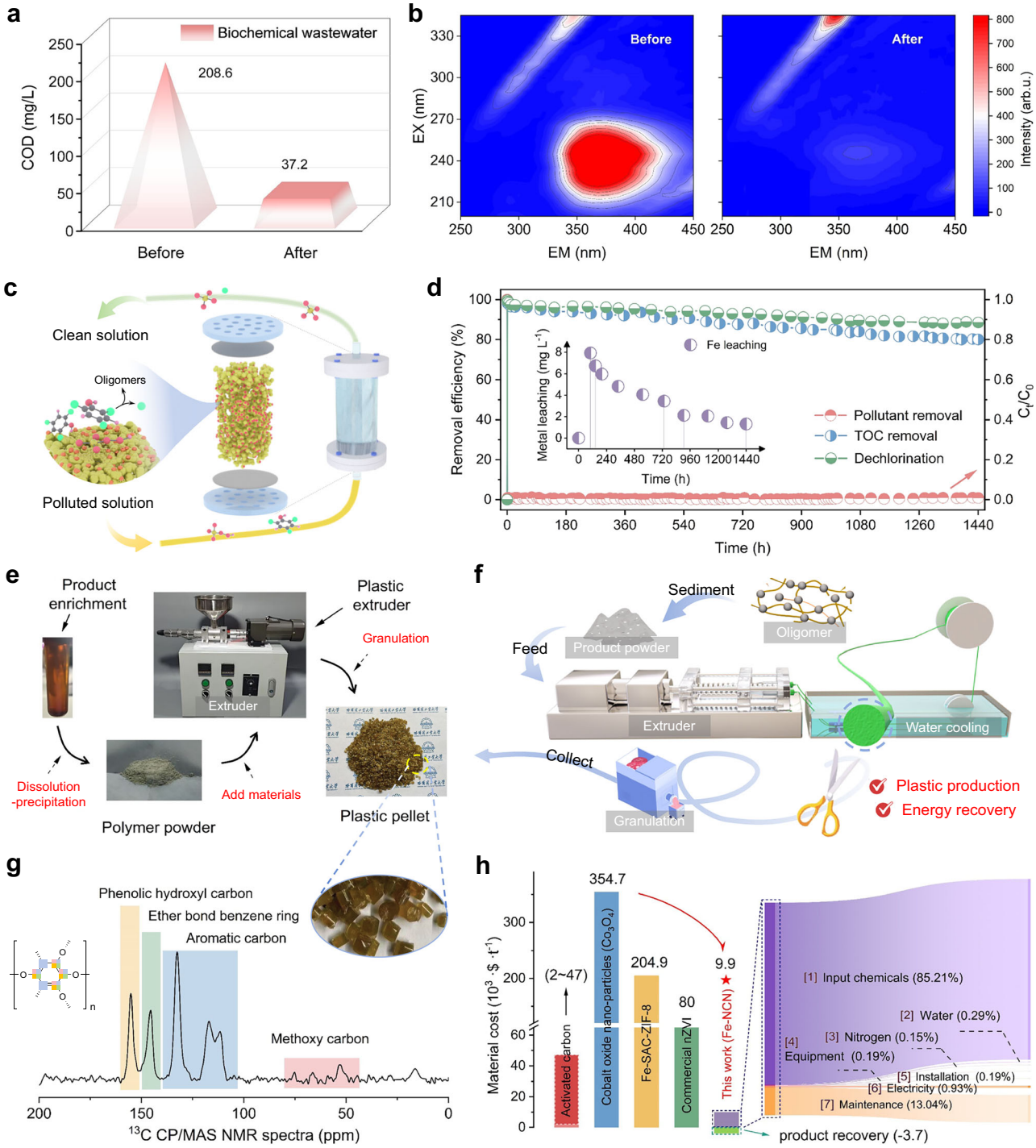

Fig. 5 | Application potential, value-added processing of products and economic and environmental feasibility of Fenton-like oxidation process. a COD changes and EEM spectra **b** before and after treatment of secondary domestic effluent from pulp and paper industry by Fe-NCN/PMS system. Experimental condition: $[pollutant]_0 = 0.1$ mM, $[PMS]_0 = 0.3$ mM, [catalyst] = 0.1 g L^{-1}, [reaction solution] = 200.0 mL. Data are presented as mean values ± s.d. (n = 2). **c** A schematic illustration of the size-enlarged catalytic reactor. **d** TCP (2.0 ppm) removal efficiency, TOC removal and dechlorination over with days in a size-enlarged catalytic reactor (inset: Fe leaching within reaction time). **e** Precipitation separation and value-added production of oligomers. **f** The industrial-grade plastic pallets are obtained through the extrusion-condensation-granulation process. **g** Solid-state ^{13}C nuclear magnetic resonance ($^{13}CNMR$) spectroscopy of plastic granules. **h** The economic feasibility of the amplified synthesis of Fe-NCN was demonstrated by technical and economic analysis (TEA). Market price data for commercial activated carbon, nano cobalt oxide, and nano zero-valent iron are sourced from the online business platform (www.made-in-china.com). Detailed plant-gate levelized costs for Fe-SAC-ZIF-8 are provided in the Supplementary Information. Source data are provided as a Source data file.

The finely modulated oxidation pathway enables the Fe-NCN/PMS system to achieve complete TCP removal, with a near-complete dechlorination rate (~99%) and polymerization conversion (~98%). The proposed pre-coordination-assisted strategy can be extended to the synthesis of other SACs (such as axially O- and S-coordinated SACs and other transition metal-based SACs), with all catalysts exhibiting excellent pollutant removal and polymerization performance (Supplementary Fig. 82). Notably, precise modulation of the

hydrophobicity and polarity of the catalytic facilitates the separation of the created oligomeric products and restores the catalyst activity. In contrast, Fe-CN lacks not only enzyme-like axial ligands to regulate the dehalogenation-polymerization transformation of TCP by metal-center-activated PMS, but also a microenvironment of enzyme-like binding pockets to regulate the transfer of the product at the active site, resulting in its lower mineralization capacity and recyclability. Fe-NCN is further integrated into a catalytic membrane reactor or a fluidized bed reactor, and excellent removal of TCP and recovery of organic carbon is achieved, highlighting the exceptional ability of Fe-NCN to deliver superior performance in continuous operation. Furthermore, high-quality plastic products were directly fabricated from pollutant-derived powdered oligomers, obtained via elution enrichment and precipitation, using an extrusion-cooling-pelletizing process. Excitingly, the economic cost of the DHP process was reduced by 25.5%, attributable to profits from the plastics (Supplementary Text 22). This underscores the substantial potential of P-AOPs for water resource recovery and value-added product generation in practical water treatment applications. However, it should be emphasized that the crosslinked C-O polymerization products exhibit a high binding affinity for the catalysts, challenging elution processes and resulting in limited product recovery (~45%). Future developments require optimizing product recovery protocols and enhancing catalyst loading capacities to advance the practical implementation of P-AOPs in large-scale applications for the selective generation and efficient recovery of high-value specific products from wastewater streams.

Methods

Synthesis of Fe-SACs

Generally, 0.18 mmol $FeSO_4 \cdot 6H_2O$ and 1,10-phenanthroline (0.027 g) were added to 10.0 mL of deionized water for 30.0 min ultrasonic treatment, and stirred at room temperature for 1.0 h to quickly form Fe^{2+}-phen chelate (red). Subsequently, it was added to a 20.0 mL solution containing dispersed 1.0 g CN (10.0 mL deionized water + 10.0 mL ethanol), stirred at room temperature for another 2.0 h, left for self-assembly overnight, and dried at 60 °C. The dried sample was thoroughly ground with 0.0347 g hydroxylamine hydrochloride in a mortar. The resulting mixture is then heated in a tube furnace to 550 °C in N_2 atmosphere at a rate of 3.3 °C/ min for 3.0 h. Finally, washing with ultra-pure water and ethanol for 3 times to remove soluble iron, drying overnight at 60 °C, Fe-NCN was collected. Fe-CN was prepared under the same conditions except that no chelating agent was added.

Melamine was heated in a tube furnace at 3.3 °C/ min in N_2 atmosphere to 550 °C for 3 h. The product collected by washing three times is named CN. Under the same pyrolysis conditions, the nitrogen-rich carbon material was prepared using phen as the precursor and named N-C.

Characterizations

XRD patterns were performed on a Rigaku MiniFlex 600 X-ray diffractometer. SEM images were collected on a FEI Quanta 450 FEG environmental scanning electron microscope. TEM images were collected on FEI Tecnai G2 Spirit TEM. HAADF-STEM images with EDS analysis were obtained on FEI Titan Themis 80-200 operating at 200 kV. Energy-dispersive X-ray spectroscopy (EDS) mapping was performed using a JEM-2100F field-emission high-resolution transmission electron microscope operated at 200 kV. Single-atom Co was characterized by AC-HAADF-STEM, and the images were captured using a JEOL JEM-2010 LaB6 high-resolution transmission electron microscope operated at 200 kV. The N_2 adsorption-desorption isotherms were obtained on a Micromeritics ASAP 2020 system to determine the Brunauer-Emmett-Teller (BET) specific surface area and pore size of catalysts. The surface elemental composition of the samples was determined by ESCA Lab 250Xi (Thermo, USA) x-ray photoelectron spectroscopy (XPS), and the Al Kα X-ray source was used for analysis, and all binding energies were calibrated using the C 1 s peak (284.8 eV). Raman spectra were measured using a Raman spectrometer (LabRAM HR Evolution, Horiba Co., Japan) equipped with a 532 nm laser. FT-IR spectroscopy spectra were collected by IR microscopy (NicoletiN10, Thermo Fisher Inc.). The EPR signals spin-trapped by DMPO and TEMP were recorded on a Bruker spectrometer (A300, Bruker, Karlsruhe, Germany) with the following settings: center field=3512 G, microwave frequency=9.86 GHz, and power = 6.36 mW.

Oxidation experiments

Fenton-like oxidation experiments of organic pollutants were carried out in a beaker. Specifically, the catalyst (0.1 g/L) was added to 50.0 mL of TCP solution (0.1 mM) mixed with 0.3 mM PMS to initiate the reaction. Unless otherwise stated, reactions were carried out at room temperature and neutral initial pH. Samples were taken periodically with a syringe, filtered through a 0.22 μm polyethersulfone membrane (1.0 mL of sample mixed with 20.0 μL sodium thiosulfate solution (0.15 mM)), and transferred to an HPLC vial. In particular, the polyethersulfone membrane needs to be pretreated to remove organic contaminants adsorbed on the membrane surface, reducing the interference of membrane adsorption on the detection of organics.

Electrochemical analysis tests

Experimental details of electrochemical analytical methods, including open circuit potentiometry (OCPT), linear scanning voltammetry (LSV), cyclic voltammetry (CV), electrochemical impedance spectroscopy (EIS), chronoamperometry (i-t), rotating ring-disk electrode experiment, and electrooxidation experiments, can be found in the Supplementary Information.

Theoretical calculation

All DFT calculations were performed using the Vienna ab initio simulation package (VASP v6.3.2)[60,61]. All MD simulations were performed by the Forcite module of the Materials Studio 20.1 software. The specific calculation details and operational parameters can be found in the Supplementary Information.

Data availability

The data supporting the findings of this study are included within the main text and the Supplementary Information files. All the raw data relevant to the study can be obtained from the corresponding author upon request. Source data are provided with this paper.

References

1. von Gunten, U. Oxidation processes in water treatment: are we on track? *Environ. Sci. Technol.* **52**, 5062–5075 (2018).
2. He, C. et al. Future global urban water scarcity and potential solutions. *Nat. Commun.* **12**, 4667–4678 (2021).
3. Huang, M. et al. Facilely tuning the intrinsic catalytic sites of the spinel oxide for peroxymonosulfate activation: from fundamental investigation to pilot-scale demonstration. *Proc. Natl. Acad. Sci. USA* **119**, e2202682119 (2022).
4. Shang, Y. et al. Single-atom catalysis in advanced oxidation processes for environmental remediation. *Chem. Soc. Rev.* **5**, 5281–5322 (2021).
5. Lee, J. et al. Persulfate-based advanced oxidation: critical assessment of opportunities and roadblocks. *Environ. Sci. Technol.* **54**, 3064–3081 (2020).
6. Zhang, Y. et al. Simultaneous nanocatalytic surface activation of pollutants and oxidants for highly efficient water decontamination. *Nat. Commun.* **13**, 3005 (2022).
7. Gao, X. et al. Carbon redirection via tunable Fenton-like reactions under nanoconfinement toward sustainable water treatment. *Nat. Commun.* **15**, 2808 (2024).

8. Liu, H. et al. Tailoring *d*-band center of high-valent metal-oxo species for pollutant removal via complete polymerization. *Nat. Commun.* **15**, 2327 (2024).
9. Liu, Y. et al. Magnesium oxide-supported single atoms with fine-modulated steric location for polymerization transfer removal of water pollutants. *Environ. Sci. Technol.* **59**, 880–891 (2024).
10. Dou, J. et al. Neglected but efficient electron utilization driven by biochar-coactivated phenols and peroxydisulfate: polyphenol accumulation rather than mineralization. *Environ. Sci. Technol.* **57**, 5703–5713 (2023).
11. Zeng, G. et al. Enhanced peroxymonosulfate activation by δ-MnO_2 nanocatalyst enriched with oxygen vacancies for phenolic pollutants polymerization. *Appl. Catal. B Environ.* **357**, 124327 (2024).
12. Saito, K. et al. Green synthesis of soluble polyphenol: oxidative polymerization of phenol in water. *Green Chem. Lett. Rev.* **1**, 47–5 (2007).
13. Kobayashi, S. et al. Oxidative polymerization of phenols revisited. *Prog. Polym. Sci.* **28**, 1015–1048 (2003).
14. Chen, Y. et al. Transformative removal of aqueous micropollutants into polymeric products by advanced oxidation processes. *Environ. Sci. Technol.* **58**, 4844–4851 (2024).
15. Gao, Z. et al. Room-temperature co-upcycling of polyvinyl chloride and polypropylene. *Nat. Sustain.* **7**, 1691–1698 (2024).
16. Palayam, M. et al. Structural insights into strigolactone catabolism by carboxylesterases reveal a conserved conformational regulation. *Nat. Commun.* **15**, 6500 (2024).
17. Sharma, S. et al. Enzymatic reaction network-driven polymerization-induced transient coacervation. *Angew. Chem. Int. Ed.* **64**, e202421620 (2025).
18. Wang, Y. et al. Unexpected activities of CYP152 peroxygenases towards non-carboxylic substrates reveal novel substrate recognition mechanism and catalytic versatility. *Angew. Chem. Int. Ed.* **137**, e202506614 (2024).
19. Zhang, Q. et al. Flavin-N_5OOH functions as both a powerful nucleophile and a base in the superfamily of flavoenzymes. *Angew. Chem. Int. Ed.* **136**, e202318629 (2024).
20. Min, Y. et al. Mimicking reductive dehalogenases for efficient electrocatalytic water dechlorination. *Nat. Commun.* **14**, 5134 (2023).
21. Chen, P. et al. Atomically dispersed iron-nitrogen species as electrocatalysts for bifunctional oxygen evolution and reduction reaction. *Angew. Chem. Int. Ed.* **56**, 610–614 (2017).
22. Song, J. et al. Directional formation of reactive oxygen species via a non-redox catalysis strategy that bypasses electron transfer process. *Adv. Mat.* **36**, 2405832 (2024).
23. Ha, M. et al. Tuning metal single atoms embedded in N_xC_y moieties toward high-performance electrocatalysis. *Energy Environ. Sci.* **14**, 3455–3468 (2021).
24. Wu, Z. et al. Facilely tuning the first-shell coordination microenvironment in iron single-atom for Fenton-like chemistry toward highly efficient wastewater purification. *Environ. Sci. Technol.* **57**, 14046–14057 (2023).
25. Peng, L. et al. Mesopore-rich Fe-N-C catalyst with FeN_4-O-NC single-atom sites delivers remarkable oxygen reduction reaction performance in alkaline media. *Adv. Mater.* **34**, 2202544 (2022).
26. Wu, Z. et al. Long-range interactions driving neighboring Fe-N_4 sites in Fenton-like reactions for sustainable water decontamination. *Nat. Commun.* **15**, 7775 (2024).
27. Wu, B. et al. Polar electric field-modulated peroxymonosulfate selective activation for removal of organic contaminants via non-radical electron transfer process. *Water Res.* **246**, 120678 (2023).
28. Zheng, W. et al. Trace Br^- inhibits halogenated by-product formation in saline wastewater electrochemical treatment. *Environ. Sci. Technol.* **58**, 12212–12224 (2024).
29. Zhang, X. et al. Nanoconfinement-triggered oligomerization pathway for efficient removal of phenolic pollutants via a Fenton-like reaction. *Nat. Commun.* **15**, 917 (2024).
30. Duan, X. et al. Nonradical reactions in environmental remediation processes: uncertainty and challenges. *Appl. Catal. B Environ.* **224**, 973–982 (2018).
31. Zhu, Z. et al. Multidimensional engineering of single-atom cobalt catalysts for ultrafast Fenton-like reactions. *Nat. Water* **3**, 211–221 (2025).
32. Song, J. et al. Asymmetrically coordinated CoB_1N_3 moieties for selective generation of high-valence Co-Oxo species via coupled electron-proton transfer in fenton-like reactions. *Adv. Mater.* **35**, 2209552 (2023).
33. Chen, F. et al. Single-atom iron anchored tubular g-C_3N_4 catalysts for ultrafast fenton-like reaction: roles of high-valency iron-oxo species and organic radicals. *Adv. Mater.* **34**, 2202891 (2022).
34. Zhao, Y. et al. Janus electrocatalytic flow-through membrane enables highly selective singlet oxygen production. *Nat. Commun.* **11**, 6228 (2020).
35. Huang, B. et al. Modulating electronic structure engineering of atomically dispersed cobalt catalyst in Fenton-like reaction for efficient degradation of organic pollutants. *Environ. Sci. Technol.* **57**, 14071–14081 (2023).
36. Wang, Y. et al. Adsorption and catalysis of peroxymonosulfate on carbocatalysts for phenol degradation: the role of pyrrolic-nitrogen. *Appl. Catal. B Environ.* **319**, 121891 (2022).
37. Miao, J. et al. Single-atom MnN_5 catalytic sites enable efficient peroxymonosulfate activation by forming highly reactive Mn (IV)–oxo species. *Environ. Sci. Technol.* **57**, 4266–4275 (2023).
38. Huang, B. et al. Coupled surface-confinement effect and pore engineering in a single-Fe-atom catalyst for ultrafast Fenton-like reaction with high-valent iron-oxo complex oxidation. *Environ. Sci. Technol.* **57**, 15667–15679 (2023).
39. Shao, P. et al. Revisiting the graphitized nanodiamond-mediated activation of peroxymonosulfate: singlet oxygenation versus electron transfer. *Environ. Sci. Technol.* **55**, 16078–16087 (2021).
40. Zhao, Y. et al. Selective activation of peroxymonosulfate govern by B-site metal in delafossite for efficient pollutants degradation: pivotal role of d orbital electronic configuration. *Water Res.* **236**, 119957 (2023).
41. Zhang, L. et al. Carbon nitride supported high-loading Fe single-atom catalyst for activation of peroxymonosulfate to generate $^1O_2$ with 100% selectivity. *Angew. Chem. Int. Ed.* **60**, 21751–21755 (2021).
42. Tang, Q. et al. Electron transfer mediated activation of periodate by contaminants to generate $^1O_2$ by charge-confined single-atom catalyst. *Nat. Commun.* **15**, 9549 (2024).
43. Ren, W. et al. Origins of electron-transfer regime in persulfate-based nonradical oxidation processes. *Environ. Sci. Technol.* **56**, 78–97 (2021).
44. Hammer, B. & Nørskov, J. Theoretical surface science and catalysis-calculations and concepts. *Adv. in Catal.* **45**, 71–129 (2000).
45. Ren, S. et al. Transforming plastics to single atom catalysts for peroxymonosulfate activation: axial chloride coordination intensified electron transfer pathway. *Adv. Mat.* **37**, 2415339 (2025).
46. Zhao, Q. et al. Rearranging spin electrons by axial-ligand-induced orbital splitting to regulate enzymatic activity of single-atom nanozyme with destructive d-π conjugation. *J. Am. Chem. Soc.* **146**, 14875–14888 (2024).
47. Li, Y. et al. Superoxide radicals mediated by high-spin Fe catalysis for organic wastewater treatment. *Proc. Natl. Acad. Sci. USA* **121**, e2407012121 (2024).
48. Zhang, Y. et al. Intrinsic strain of defect sites steering chlorination reaction for water purification. *Nat. Commun.* **16**, 2652 (2025).
49. Zong, Y. et al. Do we appropriately detect and understand singlet oxygen possibly generated in advanced oxidation processes by

electron paramagnetic resonance spectroscopy? *Environ. Sci. Technol.* **57**, 9394–9404 (2023).
50. Ji, F. et al. Excited state electronic structures and photochemistry of different oxidation states of 2, 2′-azino-bis-(3-ethylbenzothiazoline-6-sulfonic acid)(ABTS). *Spectrochim. Acta A* **253**, 119503 (2021).
51. Lister, T. et al. Engineered enzymes for enantioselective nucleophilic aromatic substitutions. *Nature* **639**, 375–381 (2025).
52. Gómez-Gallego, M. & Sierra, M. A. Kinetic isotope effects in the study of organometallic reaction mechanisms. *Chem. Rev.* **111**, 4857–4963 (2011).
53. Yao, Z. et al. High-entropy alloys catalyzing polymeric transformation of water pollutants with remarkably improved electron utilization efficiency. *Nat. Commun.* **16**, 148 (2025).
54. Du, L. et al. Direct detection of the open-shell singlet phenyloxenium ion: an atom-centered diradical reacts as an electrophile. *J. Am. Chem. Soc.* **139**, 15054–15059 (2017).
55. Vigalok, A. et al. Metal-stabilized phenoxonium cation. *J. Am. Chem. Soc.* **125**, 15692–15693 (2003).
56. Baesjou, P. et al. Ab initio calculations on 2,6-dimethylphenol and 4-(2,6-dimethylphenoxy)–2,6-dimethylphenol. Evidence of an important role for the phenoxonium cation in the coppercatalyzed oxidative phenol coupling reaction. *J. Am. Chem. Soc.* **119**, 12590–12594 (1997).
57. Duan, P. et al. Polymeric products deactivate carbon-based catalysts in catalytic oxidation reactions. *Nat. Water* **3**, 178–190 (2025).
58. Liu, Y. et al. Biomimetic hydrophobic-polar metal-organic frameworks for record-breaking separation and capture of xenon and krypton. *Angew. Chem. Int. Ed.* **64**, e20094 (2025).
59. Pi, Z. et al. Complete degradation of 2, 4-dichlorophenol in a sequential sulfidated nanoscale zero-valent iron/peroxydisulfate system: dechlorination, mineralization and mechanism. *Environ. Sci. Nano* **12**, 1414–1430 (2025).
60. Perdew, J. et al. Generalized gradient approximation made simple. *Phys. Rev. Lett.* **77**, 3865–3868 (1996).
61. Blöchl, P. E. Projector augmented-wave method. *Phys. Rev. B* **50**, 17953–17979 (1994).
62. Momma, K. & Izumi, F. VESTA3 for three-dimensional visualization of crystal, volumetric and morphology data. *J. Appl. Crystallogr.* **44**, 1272–1276 (2011).

Acknowledgements

This research gratefully acknowledges funding from the National Natural Science Foundation of China (No. 52370163), National Key Research and Development Program of China (No. 2022YFA0912501), State Key Laboratory of Urban-rural Water Resourcesand Environment (Harbin Institute of Technology) (No. 2025DX12). The authors extend their gratitude to Theoretical and Computational Chemistry Team (from Scientific Compass www.shiyanjia.com) for providing invaluable assistance. Furthermore, we extend our sincere gratitude to Dr Y.Z. (Yingjie Zhang) from the University of Science and Technology of China and Dr J.M. (Jie Miao) from Nanjing Tech University for their invaluable assistance in experimental work and characterization.

Author contributions

B.W. and Z.L. designed the research. B.W. carried out the experiments and drafted the manuscript. J.Z. and W.Z. assisted with experiments and characterization. S.H. contributed novel reagents/analytical tools. Z.L., X.D., and A.W. further revised the manuscript. Z.L., X.D., and A.W. supervised the project. All authors contributed to the discussion in the manuscript.

Competing interests

The authors declare no competing interests.

Additional information

Supplementary information The online version contains supplementary material available at https://doi.org/10.1038/s41467-026-69253-y.

Correspondence and requests for materials should be addressed to Zhiling Li, Xiaoguang Duan or Aijie Wang.

Peer review information *Nature Communications* thanks the anonymous reviewers for their contribution to the peer review of this work. A peer review file is available.

Reprints and permissions information is available at http://www.nature.com/reprints

Publisher's note Springer Nature remains neutral with regard to jurisdictional claims in published maps and institutional affiliations.

Open Access This article is licensed under a Creative Commons Attribution-NonCommercial-NoDerivatives 4.0 International License, which permits any non-commercial use, sharing, distribution and reproduction in any medium or format, as long as you give appropriate credit to the original author(s) and the source, provide a link to the Creative Commons licence, and indicate if you modified the licensed material. You do not have permission under this licence to share adapted material derived from this article or parts of it. The images or other third party material in this article are included in the article's Creative Commons licence, unless indicated otherwise in a credit line to the material. If material is not included in the article's Creative Commons licence and your intended use is not permitted by statutory regulation or exceeds the permitted use, you will need to obtain permission directly from the copyright holder. To view a copy of this licence, visit http://creativecommons.org/licenses/by-nc-nd/4.0/.

© The Author(s) 2026

[1]State Key Laboratory of Urban-rural Water Resource and Environment, School of Environment, Harbin Institute of Technology, Harbin, PR China. [2]School of Chemical Engineering, The University of Adelaide, Adelaide, SA, Australia. [3]State Key Laboratory of Urban Water Resource and Environment, School of Civil and Environmental Engineering, Harbin Institute of Technology Shenzhen, Shenzhen, PR China. ✉e-mail: lizhiling@hit.edu.cn; xiaoguang.duan@adelaide.edu.au; wangaijie@hit.edu.cn